Atmospheric
Chemistry
and Physics

Supplement of

Contribution of the world's main dust source regions to the global cycle of desert dust

Jasper F. Kok et al.

Correspondence to: Jasper F. Kok (jfkok@ucla.edu)

This document contains Supplementary Methods (i) describing an analysis of possible systematic errors in the attribution of the global dust cycle to the different source regions, (ii) describing how results of the seasonal dust emission, loading, and DAOD per source region were obtained from AeroCom Phase I simulations, and (iii) describing how the size-resolved attribution of the global dust cycle to the different dust source regions was obtained. In addition, this document contains a number of Supplementary Figures, which are summarized below:

- Figures S1-S4. Fractional contribution of each source region to the global dust cycle in respectively boreal Winter (DJF), Spring (MAM), Summer (JJA), and Fall (SON).
- Figure S5. Annual size-resolved lifetime of dust emitted from each of the nine source regions, as simulated by the six models in the model ensemble.
- Figures S6-S9. Size-resolved lifetime of dust emitted from each of the nine source regions in respectively Winter, Spring, Summer, and Fall.
- Figure S10. The column-integrated bulk mass extinction efficiency (m^2/g) due to dust from all source regions.
- Figure S11. Attribution of the annually averaged PM20 dust loading to the world's main source regions.
- Figures S12-S15. Attribution of the 2D dust aerosol optical depth in respectively boreal Winter (DJF), Spring (MAM), Summer (JJA), and Fall (SON) to the world's main source regions.
- Figures S16-S19. Attribution of the 2D dust column loading in respectively boreal Winter (DJF), Spring (MAM), Summer (JJA), and Fall (SON) to the world's main source regions.
- Figures S20-S23. Attribution of the zonally averaged dust concentration to the world's main source regions in respectively boreal Winter (DJF), Spring (MAM), Summer (JJA), and Fall (SON).
- Figure S24. Map of regions to which deposition fluxes are quantified in the main text.
- Figure S25-28. Attribution to the world's main source regions of the seasonally-averaged PM20 dust deposition flux in respectively boreal Winter (DJF), Spring (MAM), Summer (JJA), and Fall (SON).
- Figure S29. Correction factors needed per source region to optimize agreement against compilations of surface concentration and deposition flux measurements.

Supplementary Methods

Analysis of seasonal dust cycle in AeroCom simulations

We obtain estimates of the seasonally-averaged dust loading ($\tilde{L}_{r,s}^{\text{Aer}}$) and DAOD ($\tilde{\tau}_{r,s}^{\text{Aer}}$) for each of the models in the AeroCom Phase I ensemble by following the procedure in Section 2.2 of the main text. That is,

$$\tilde{L}_{r,s}^{\text{Aer}} = \tilde{F}_{r,s}^{\text{Aer}} \tilde{T}_{\text{glob}}^{\text{Aer}} \frac{\breve{T}_{r,s}}{\breve{T}_{\text{glob}}}, \text{ and} \tag{S.1}$$

$$\tilde{\tau}_{r,s}^{\text{Aer}} = \frac{\tilde{L}_{r,s}^{\text{Aer}}}{A_{\text{Earth}}} \breve{\epsilon}_{\text{glob}}^{\text{Aer}} \frac{\breve{\epsilon}_{r,s}}{\breve{\epsilon}_{\text{glob}}}, \tag{S.2}$$

where $\breve{T}_{r,s}$ and $\breve{\epsilon}_{r,s}$ are respectively the bulk lifetime for source region r and season s, obtained from our analysis.

Size-resolved attribution of the global dust cycle to the different dust source regions

Following Eqs. (1)-(4) in the main text, the size-resolved fractional contributions of each source region to DAOD ($\check{f}_{\tau_{r,s,k}}$), dust column loading ($\check{f}_{l_{r,s,k}}$), dust concentration ($\check{f}_{C_{r,s,k}}$), and dust deposition flux ($\check{f}_{D_{r,s,k}}$) are

$$\check{f}_{\tau_{r,s,k}} = \check{\tau}_{r,s,k} / \sum_{r=1}^{N_{sreg}} \check{\tau}_{r,s,k}, \tag{S.3}$$

$$\check{f}_{l_{r,s,k}} = \check{l}_{r,s,k} / \sum_{r=1}^{N_{sreg}} \check{l}_{r,s,k}, \tag{S.4}$$

$$\check{f}_{C_{r,s,k}} = \check{C}_{r,s,k} / \sum_{r=1}^{N_{sreg}} \check{C}_{r,s,k}, \tag{S.5}$$

$$\check{f}_{D_{r,s,k}} = \check{D}_{r,s,k} / \sum_{r=1}^{N_{sreg}} \check{D}_{r,s,k}, \tag{S.6}$$

where $\check{\tau}_{r,s,k}$, $\check{l}_{r,s,k}$, $\check{C}_{r,s,k}$, and $\check{D}_{r,s,k}$ are the contributions of each source region r to respectively the DAOD, loading, concentration, and total (dry and wet) deposition flux in season s for different particle size bins (subscript k) spanning $0.2 - 0.5$, $0.5 - 1.0$, $1.0 - 2.5$, $2.5 - 5.0$, $5.0 - 10$, and $10 - 20$ μm particle bin k (see Kok et al. (2021) for the exact methodology).

Realism of errors in the fractional contributions of different source regions to the global dust cycle

In our companion article we showed that the errors on the inverse model results summed over all source regions are consistent within the uncertainties with independent measurements of surface concentration and deposition flux (see Figs. 7 and 10 in Kok et al., 2021). Here, we inform whether our errors on the contribution per source region are realistic by determining the optimal correction factor per source region that minimizes the disagreement against the independent data sets of surface concentration and deposition flux. Specifically, we obtained the values of the source region-specific correction factors γ_r that minimizes the cost function of the squared deviation (χ^2) between the inverse model results and the measurements,

$$\chi^2 = \sum_{i=1}^{N_i} M_i - \sum_{r=1}^{N_{sreg'}} \check{f}_{r,i} \gamma_r \breve{M}_i \tag{S.7}$$

where N_i is the number of observational data in either the annual surface concentration or deposition flux data set, M_i is the ith measured value in the data sets of either annual surface concentration or deposition flux used in Kok et al. (2021), $\breve{M}_i$ is the corresponding inverse model result for the same location, and $\check{f}_{r,i}$ is the fractional contribution to $\breve{M}_i$ of each source region r. In minimizing the cost function χ^2, we grouped both the North African source regions (western North Africa, eastern North Africa, and the Sahel) and the Asian source regions (Middle East & Central Asia), as for instance the absence of concentration stations near the eastern North Africa and Middle East & Central Asia source regions (Fig. 2c in Kok et al., in review) otherwise causes overfitting. We furthermore set the correction factor γ_r for North America equal to 1 to avoid overfitting as none of the concentration stations are dominated by this

source region. The number of source regions N_{sreg}' used in Eq. (S.7) therefore equals 5. The fractional contribution of each dust source region to global dust loading then equals

$$f_{L_r} = \gamma_r \breve{L}_r / \sum_{r=1}^{N_{\text{sreg}}'} \gamma_r \breve{L}_r \qquad (S.8)$$

where $\breve{L}_r$ is the annual global loading per source region that produces optimal results against DAOD constraints as obtained by the inverse model (see Kok et al., 2021). Similar results can be obtained for the fractional contribution of each source region to global dust emissions and global DAOD, which are not shown here because these results are nearly identical to those obtained from Eq. (S.8).

This analysis yields a few insights (Figs. 9 and S29). First, the relative contribution of North African and Asian source regions is consistent with surface concentration data as the probability distributions of the optimal values of the correction factors γ_r are centered around 1. However, the correction factor for Asian source regions that maximizes agreement against deposition data is larger than 1, such that a larger fractional contribution of Asian source regions is needed to maximize agreement with deposition flux measurements. This might suggest that inverse model results underestimate Asian dust, which we already find is more abundant than accounted for in most models (see section 3.1). Furthermore, correction factors for the Southern Hemisphere source regions are slightly smaller than 1 with respect to concentration data and larger than 1 with respect to deposition data. This inconsistency between comparisons against SH surface concentration and deposition flux measurements was already noted in Kok et al. (2021).

Supplementary Figures
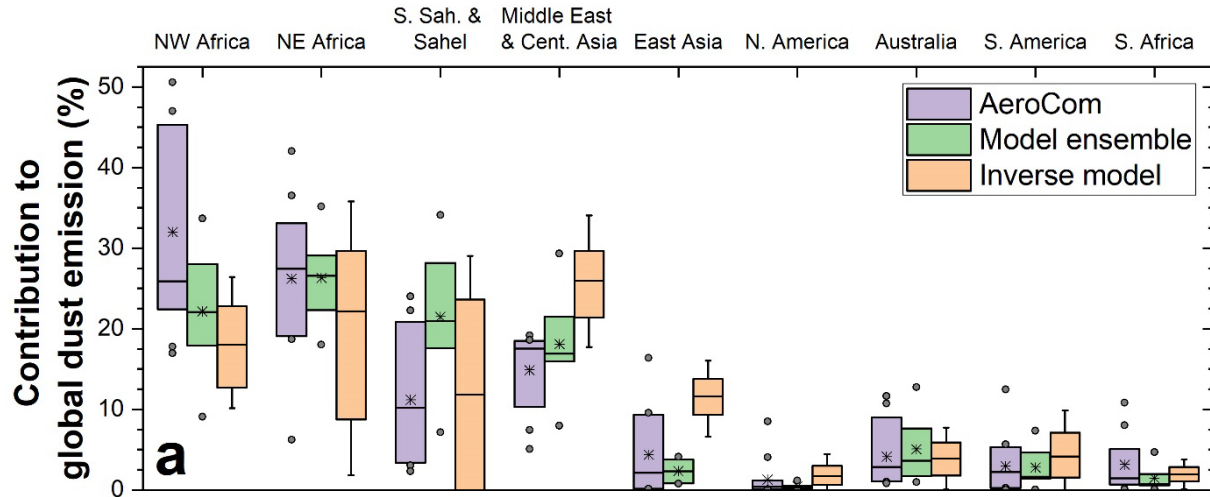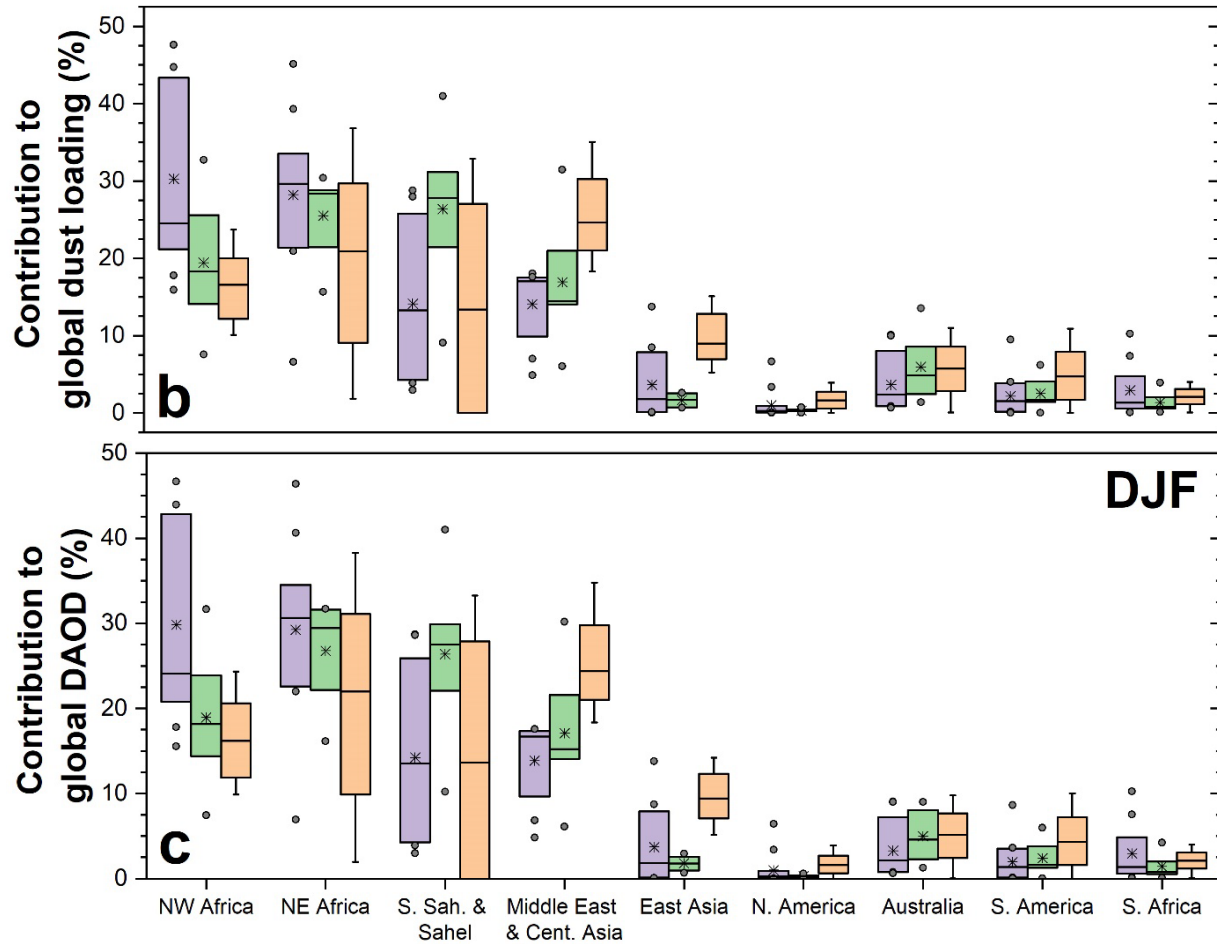
Figure S1. Fractional contribution of each source region to the global dust cycle in boreal Winter (DJF). Shown are the fractional contributions to the global dust emission (and deposition) flux (**a**), the global dust loading (**b**), and the global dust aerosol optical depth (**c**). Box boundaries approximately denote the one standard error range (i.e., contains 9 out of 13 AeroCom simulations, 4 out of 6 model ensemble members, and 68% probability range for the inverse model's results), gray circles denote the individual simulation results outside of this range, whiskers denote the 95% confidence interval for the inverse model's results, horizontal solid lines denote the median result, and stars denote the mean result.
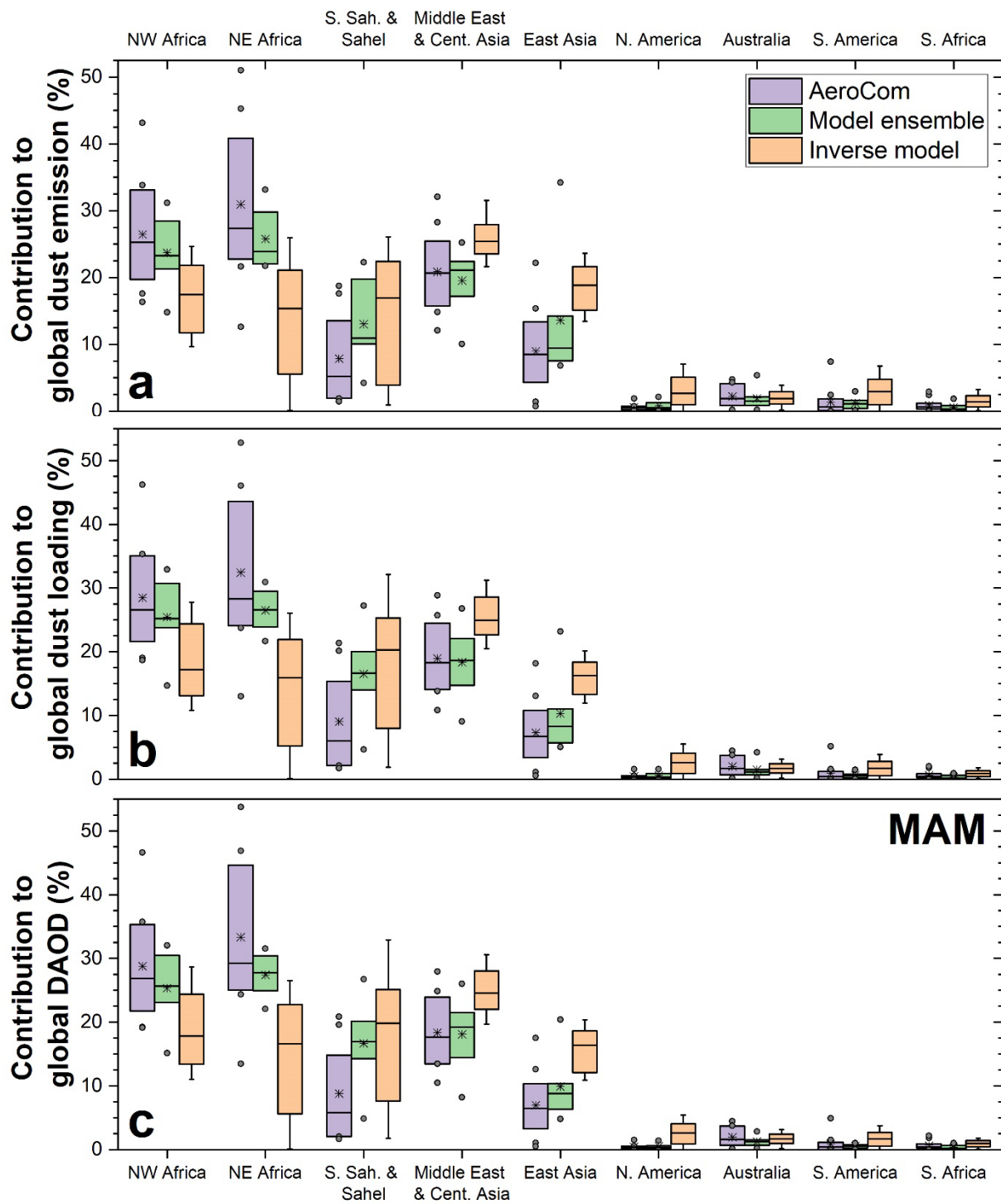
Figure S2. As in Figure S1, but for the fractional contribution of each source region to the global dust cycle in boreal Spring (DJF).
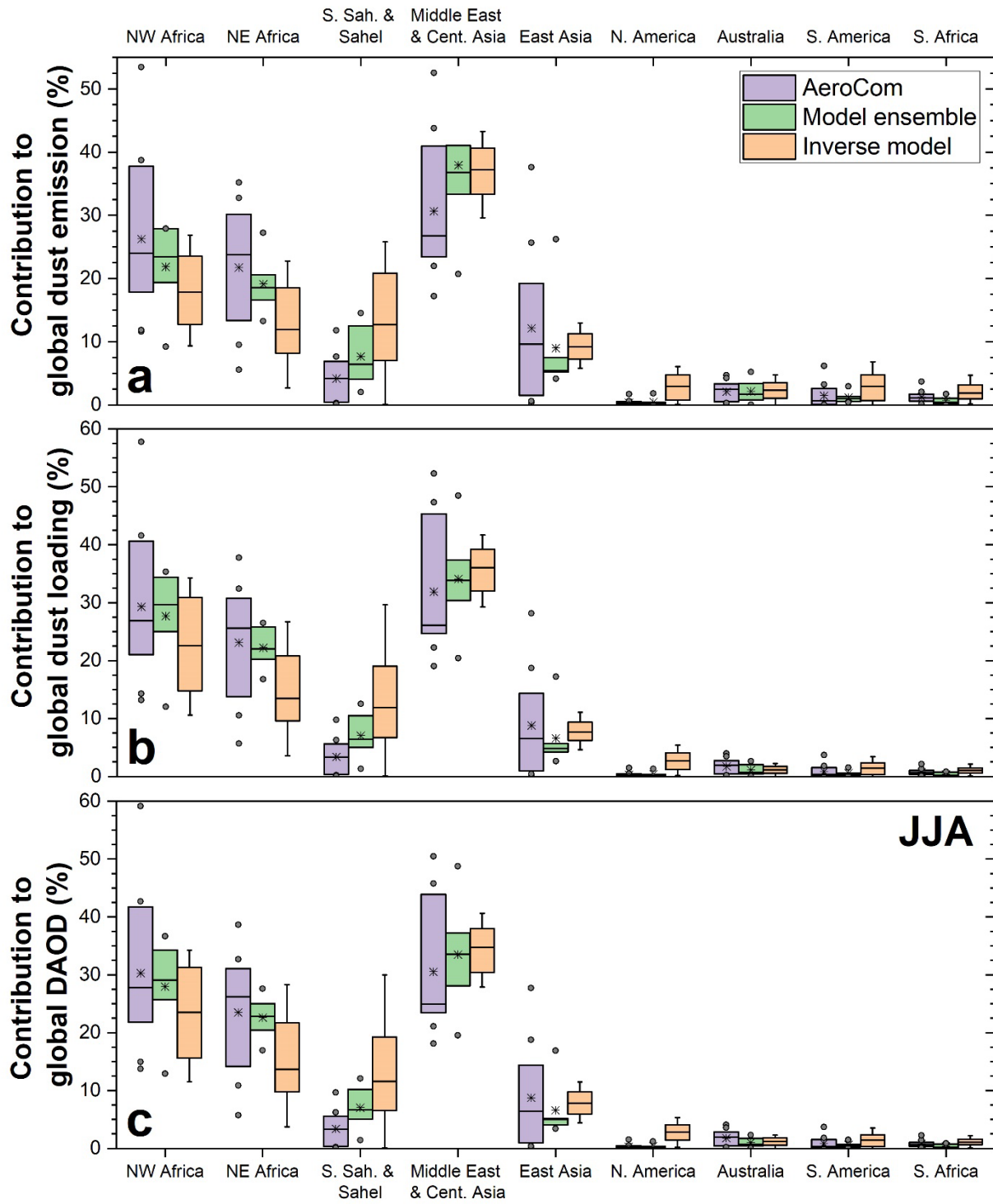
Figure S3. As in Figure S1, but for the fractional contribution of each source region to the global dust cycle in boreal Summer (JJA).
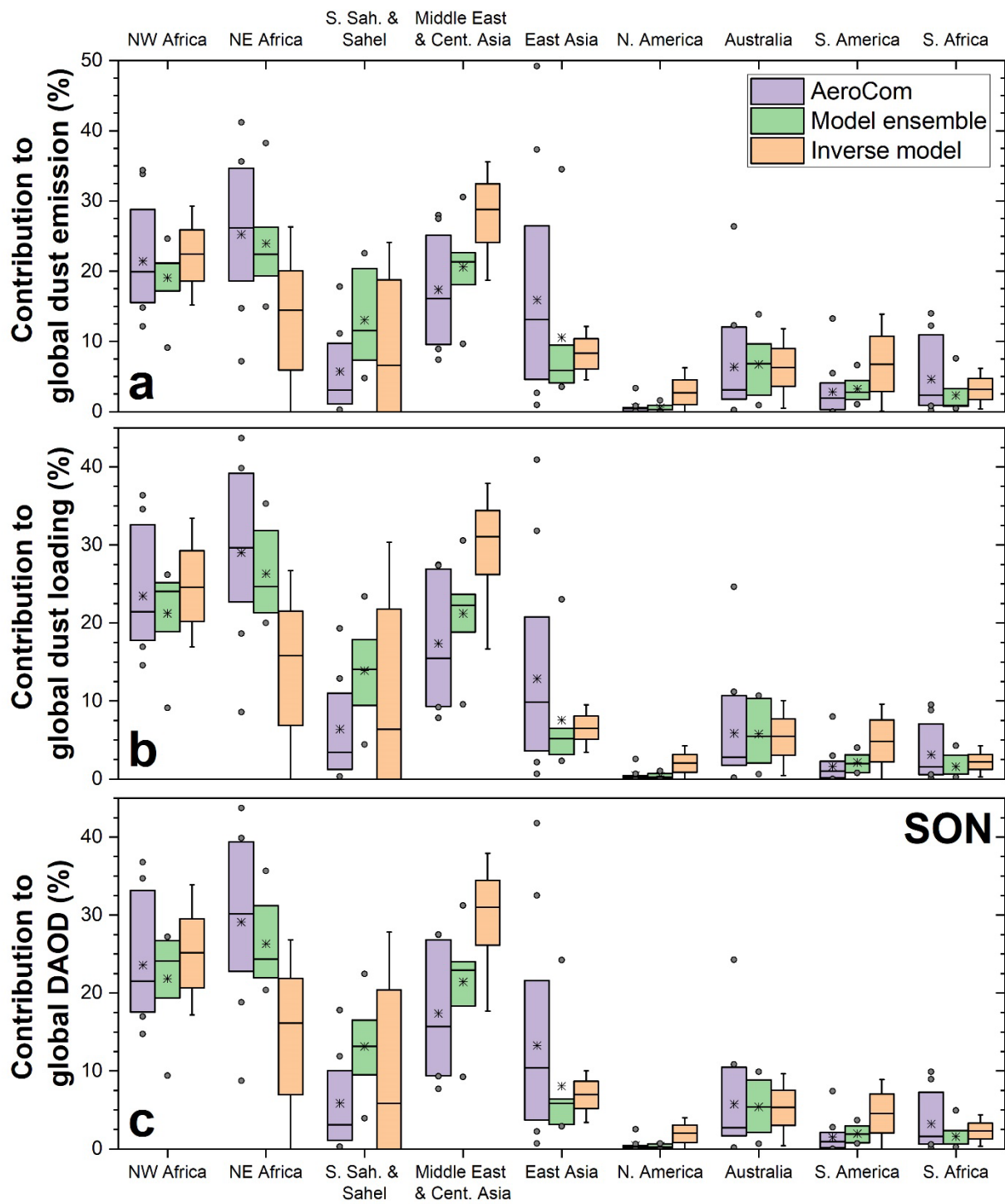
Figure S4. As in Figure S1, but for the fractional contribution of each source region to the global dust cycle in boreal Fall (SON).
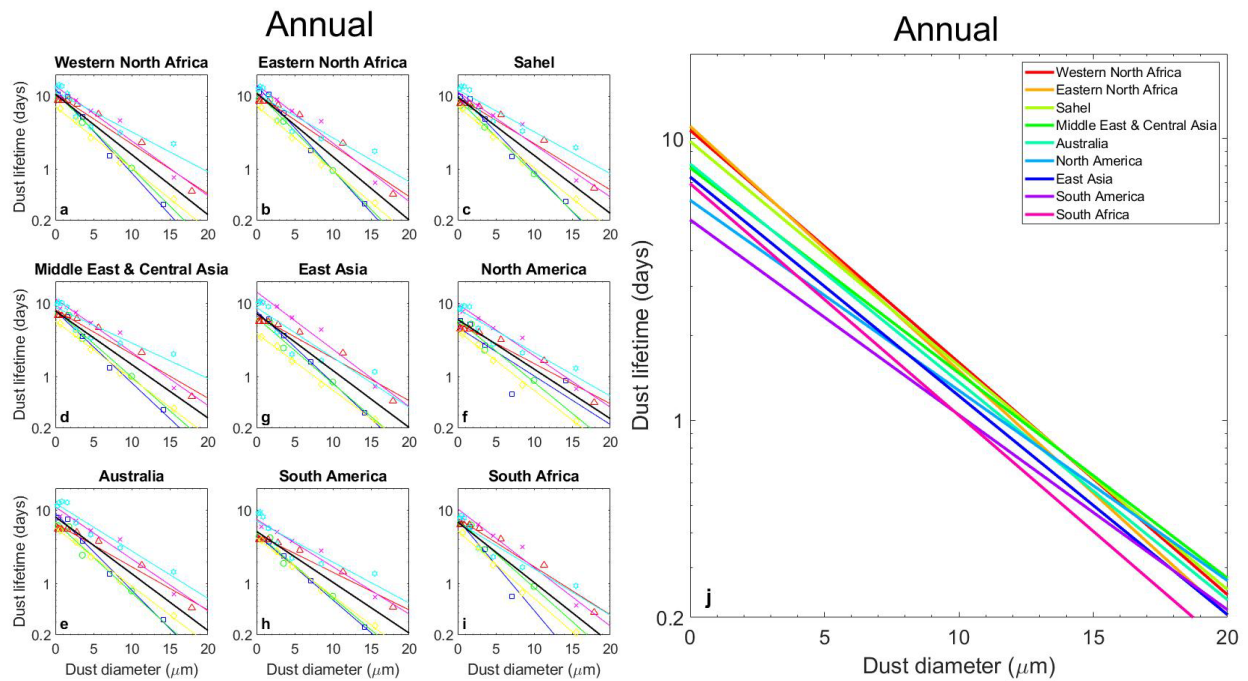
Figure S5. Annual size-resolved lifetime of dust emitted from each of the nine source regions, as simulated by the six models in the model ensemble (CESM = blue squares; IMPACT = green circles; GISS = red triangles; GOCART = purple crosses; MONARCH = cyan hexagons; INCA = yellow diamonds). Also shown are the Maximum Likelihood Estimates (MLE) of the best fit for each region (black lines), which uses data from all the models and were obtained as described in the Supplement to Kok et al. (2017). To facilitate comparisons between source regions, panel (j) shows the MLEs of the size-resolved lifetime for the nine regions.
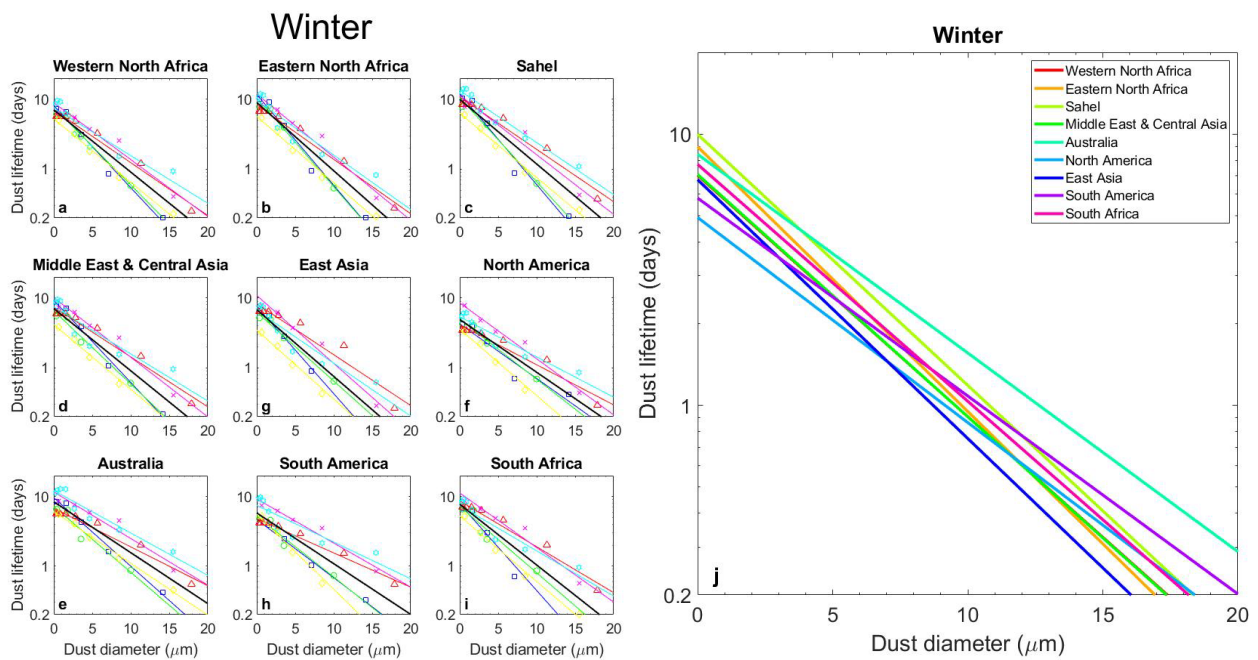
Figure S6. Size-resolved lifetime of dust emitted from each of the nine source regions in Winter (December – February for Northern Hemisphere sources; June – August for Southern Hemisphere sources), as simulated by the six models in the model ensemble (CESM = blue squares; IMPACT = green circles; GISS = red triangles; GOCART

= purple crosses; MONARCH = cyan hexagons; INCA = yellow diamonds). Also shown are the Maximum Likelihood Estimates (MLE) of the best fit for each region (black lines), which uses data from all the models and were obtained as described in the Supplement to Kok et al. (2017). To facilitate comparisons between source regions, panel (j) shows the MLEs of the size-resolved lifetime for the nine regions.
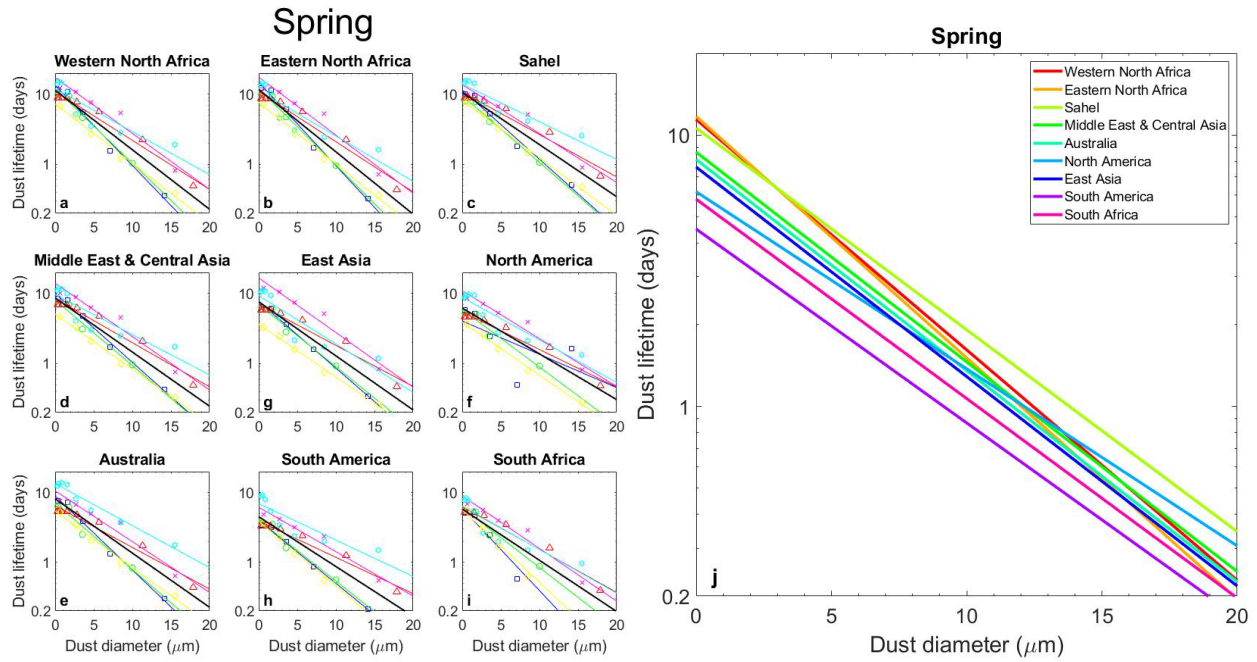
Figure S7. As in Figure S6, but for the size-resolved dust lifetime in Spring (March – May for Northern Hemisphere sources; September – November for Southern Hemisphere sources).
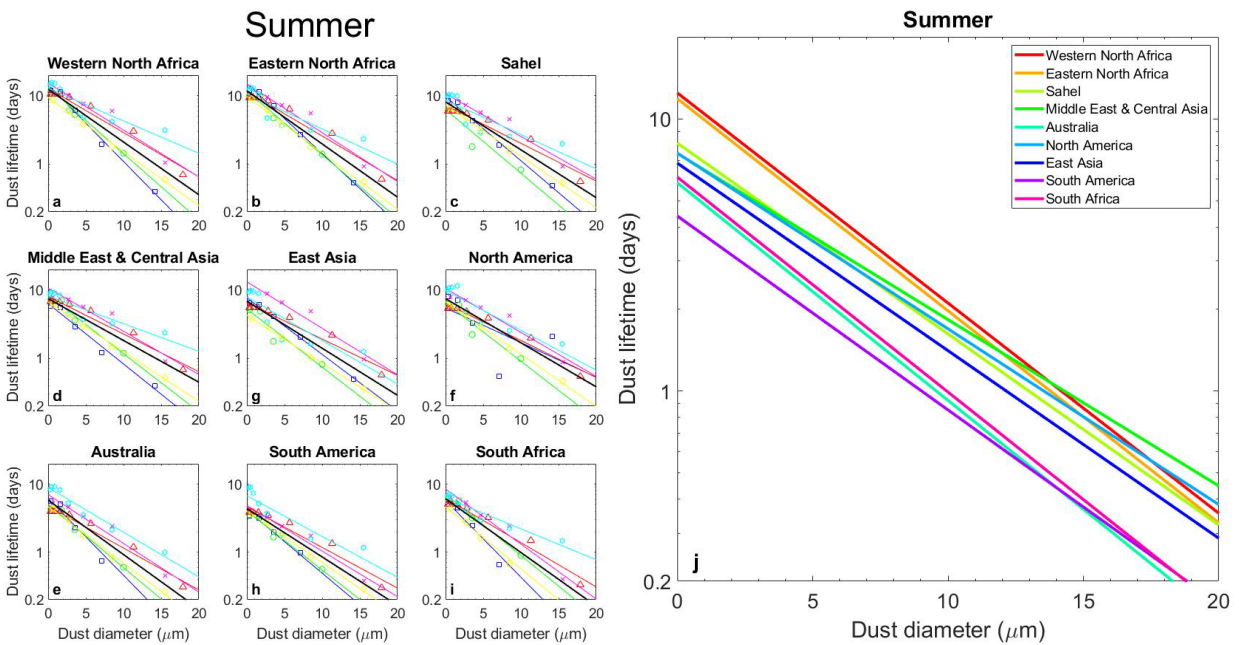
Figure S8. As in Figure S6, but for the size-resolved dust lifetime in Spring (March – May for Northern Hemisphere sources; September – November for Southern Hemisphere sources).
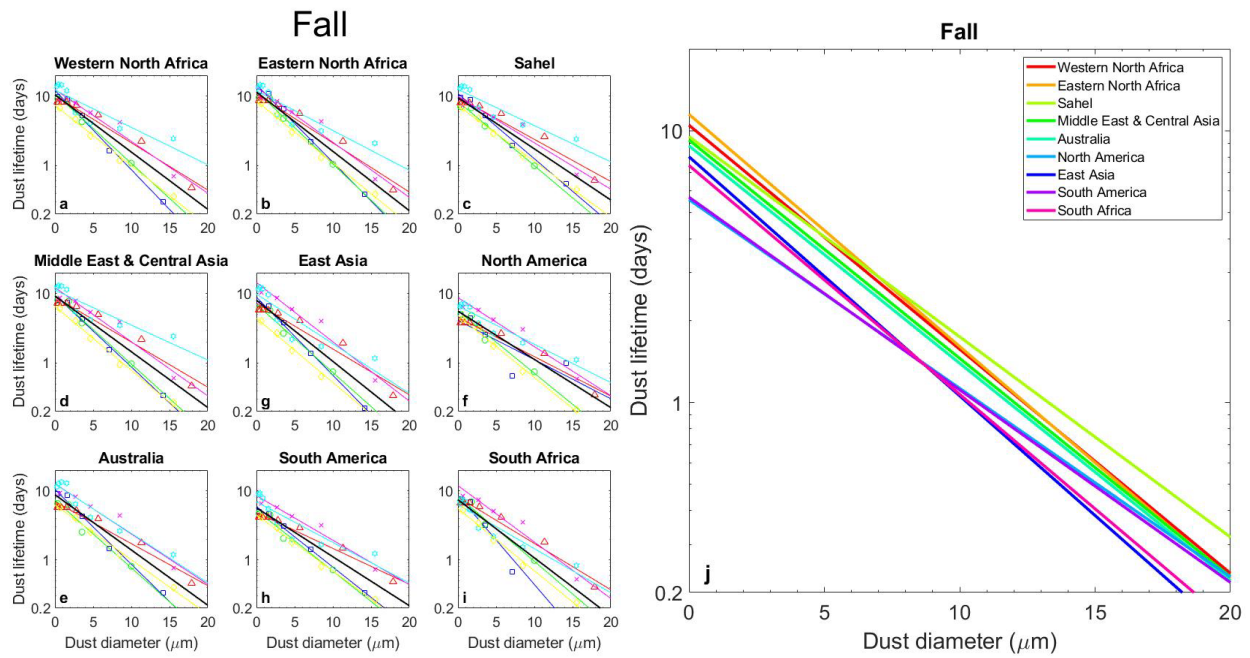
Figure S9. As in Figure S6, but for the size-resolved dust lifetime in Spring (March – May for Northern Hemisphere sources; September – November for Southern Hemisphere sources).
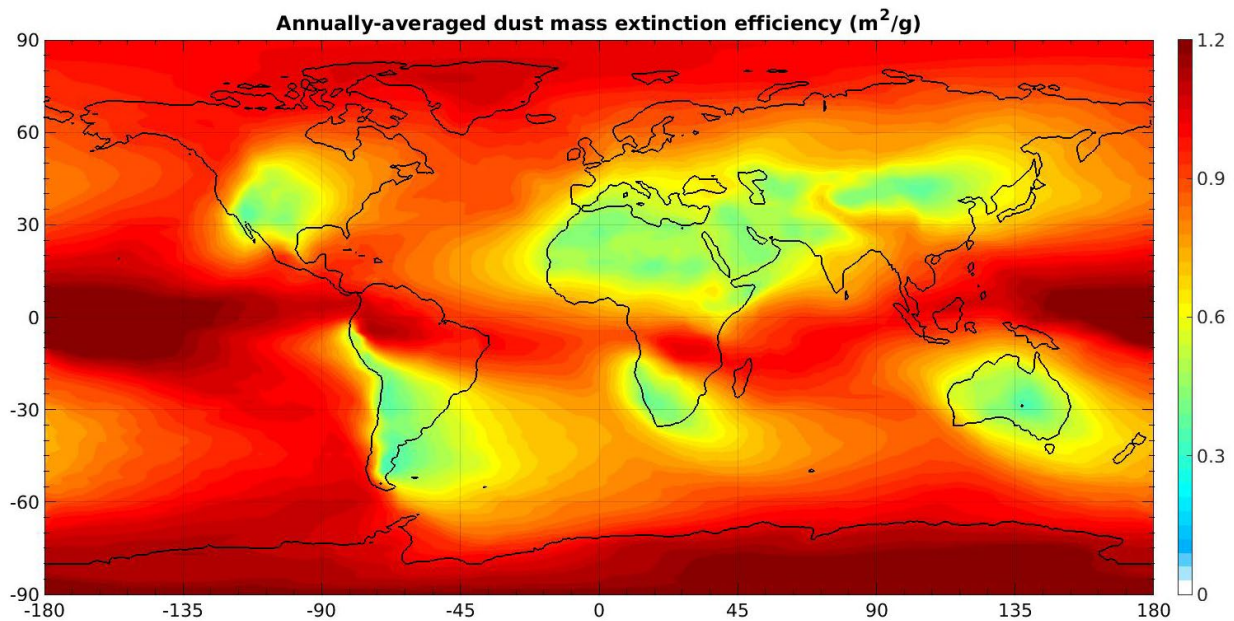
Figure S10. The column-integrated bulk mass extinction efficiency (m^2/g) due to dust from all source regions.
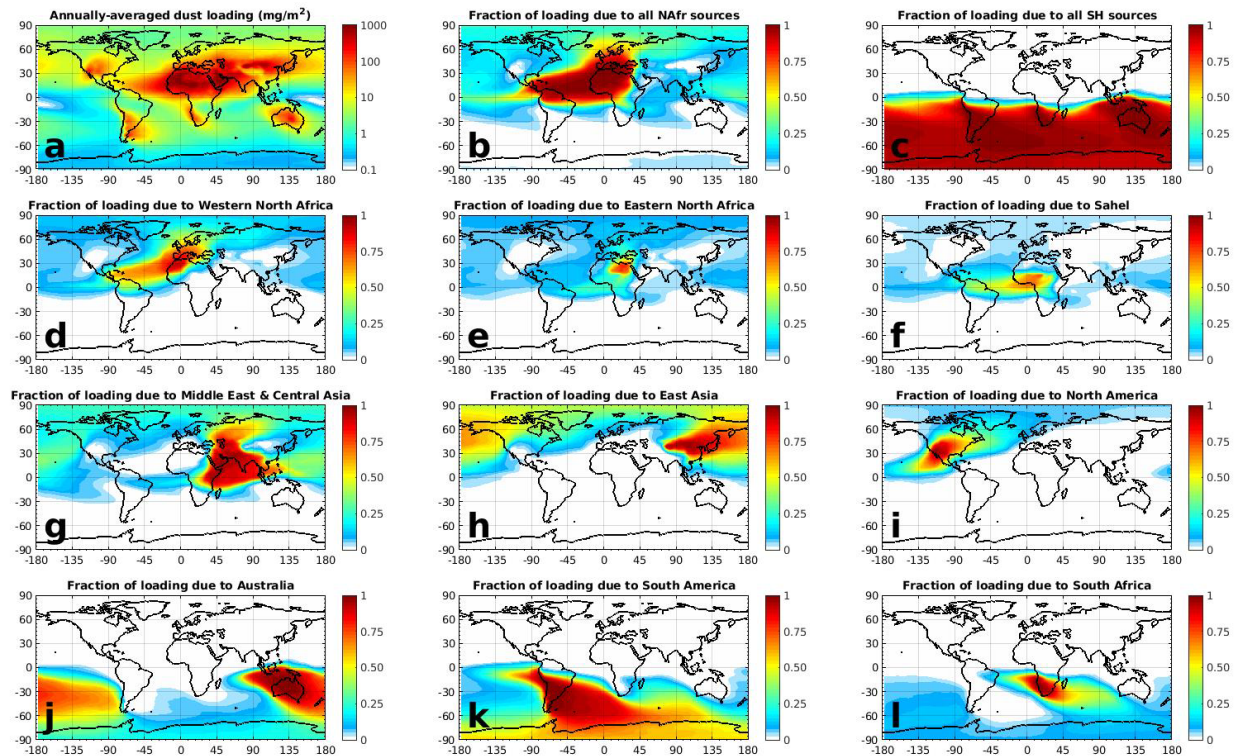
Figure S11. Attribution of the annually averaged PM$_{20}$ dust loading to the world's main source regions. Panel ordering is identical to Figure 5 and the seasonally resolved attribution of dust loading is shown in Figures S15-S18.
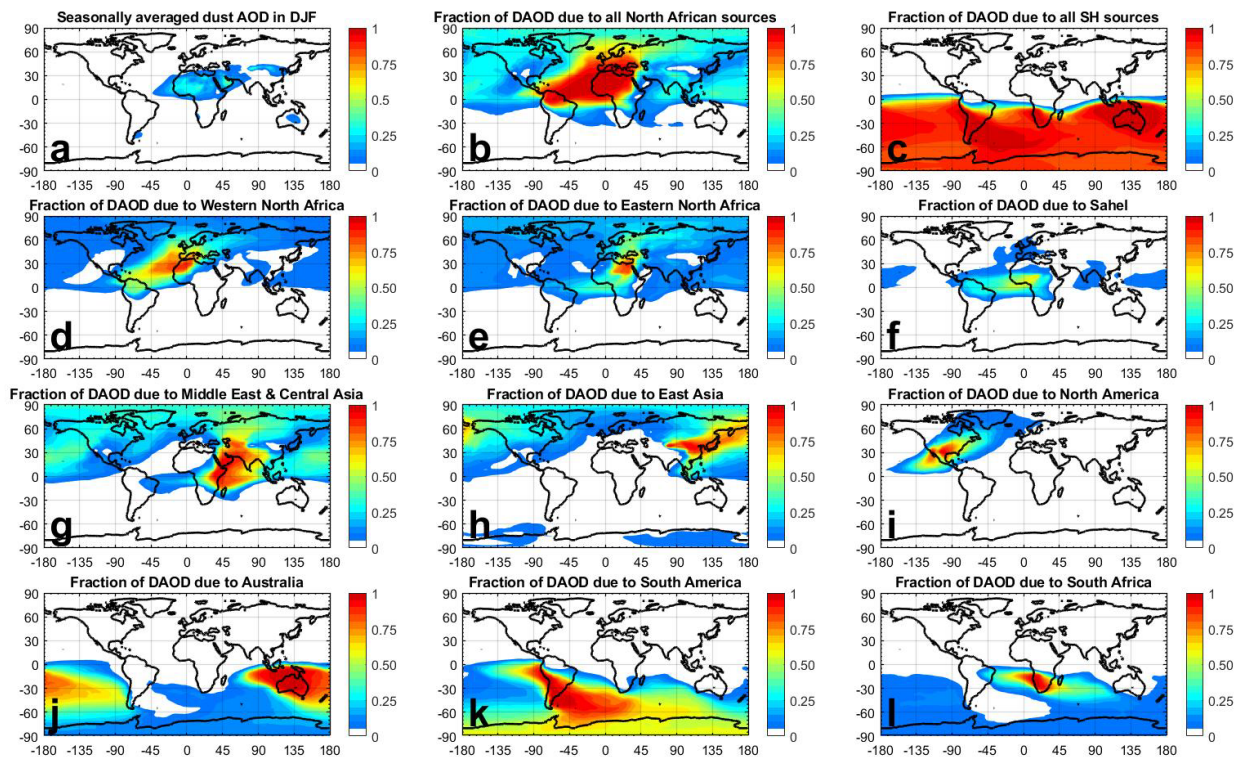
Figure S12. Attribution of the 2D dust aerosol optical depth in boreal winter (DJF) to the world's main source regions. Shown first is the seasonally-averaged DAOD produced from all source regions combined (a), followed by

the fraction of DAOD that is due to Northern Hemisphere (b) and North African (c) sources. The fraction of DAOD due to each of the three North African source regions are shown in panels (d)-(f), and the fraction of DAOD due to the other three Northern Hemisphere source regions of Middle East & Central Asia, East Asia, and North America are showns in panels (g)-(i). Finally, the fraction of 2D DAOD due to the three Southern Hemisphere source regions of Australia, South America, and South Africa are shown in panels (j)-(l).
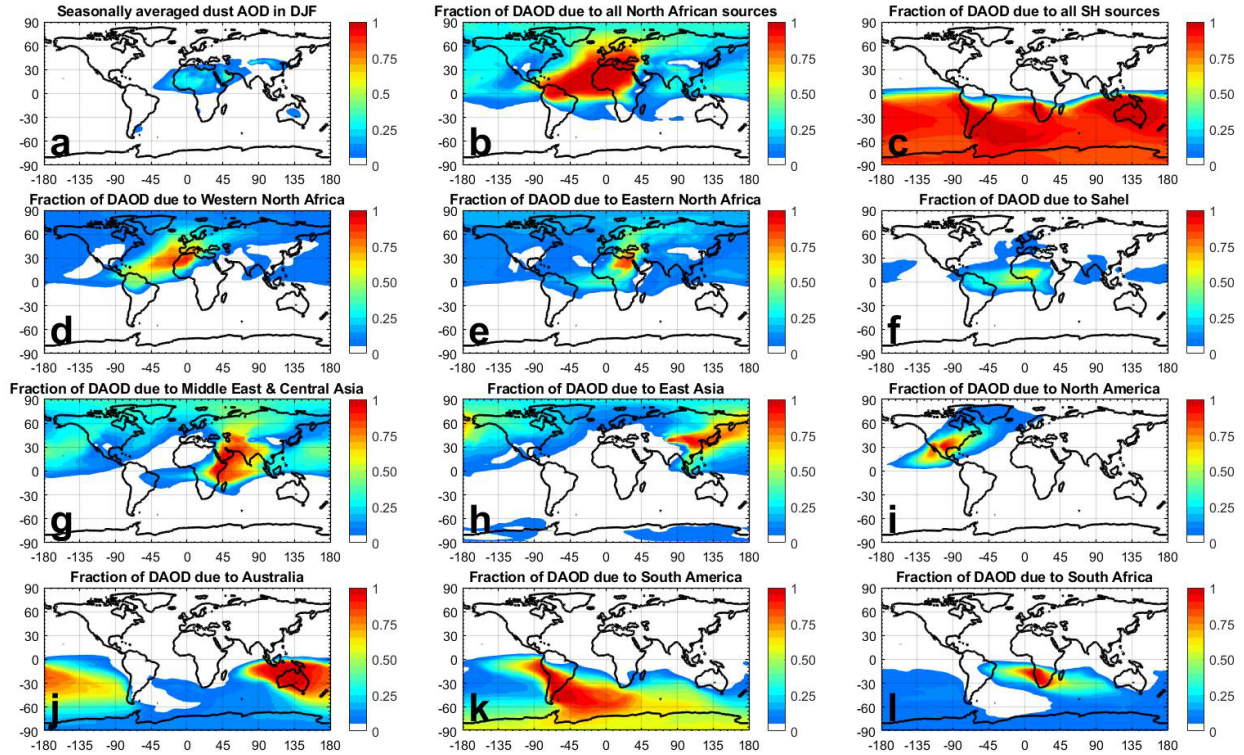
Figure S13. As in Figure S12, but for the attribution of the 2D dust aerosol optical depth in boreal Spring (MAM).
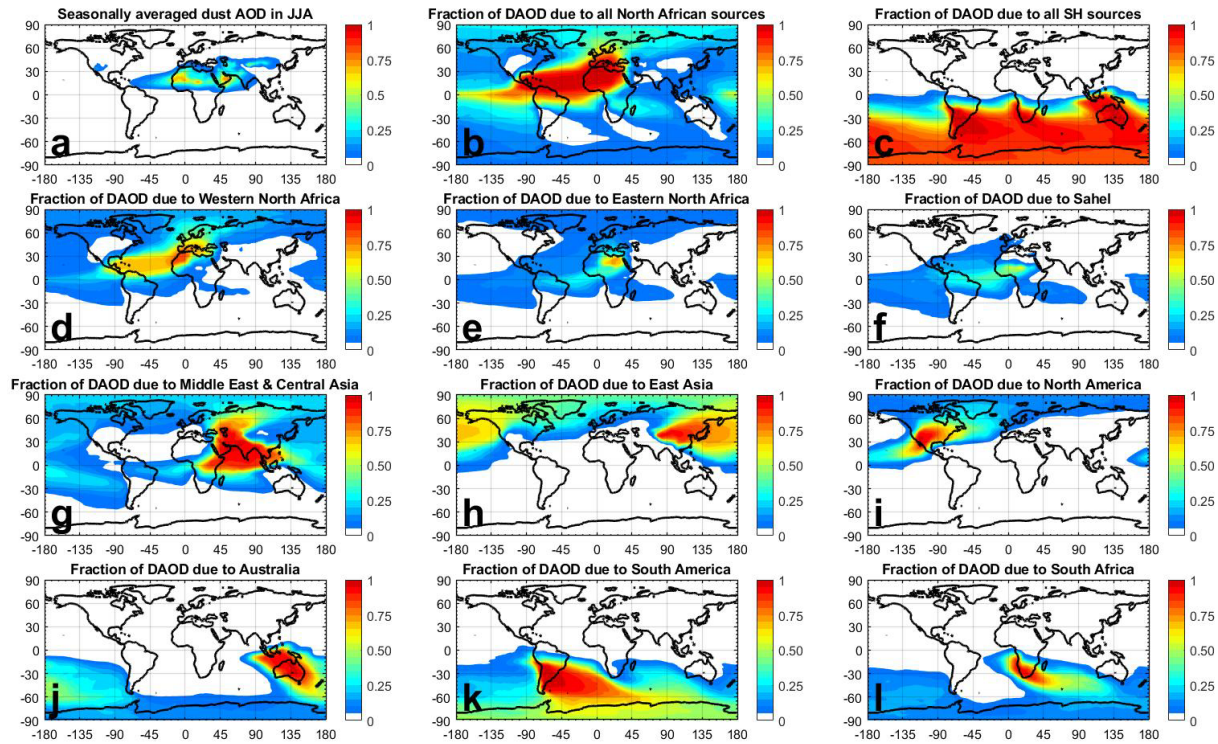
Figure S14. As in Figure S12, but for the attribution of the 2D dust aerosol optical depth in boreal Summer (JJA).
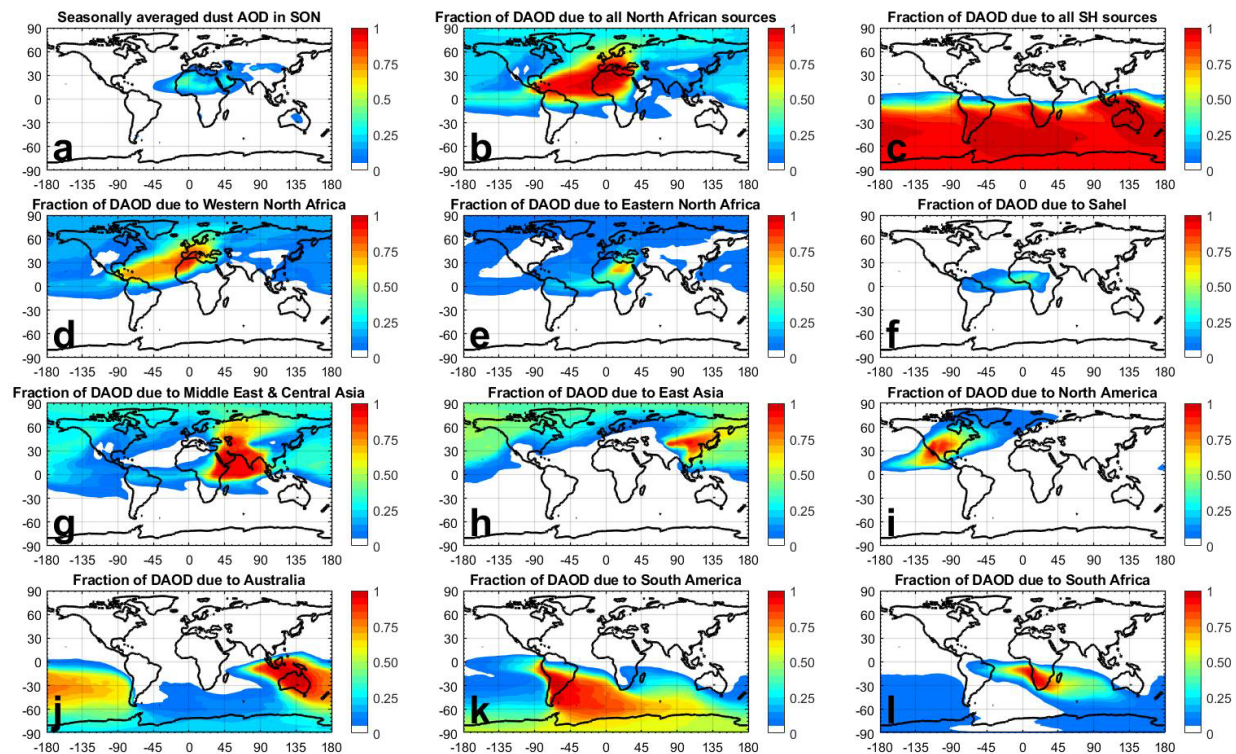
Figure S15. As in Figure S12, but for the attribution of the 2D dust aerosol optical depth in boreal Fall (SON).
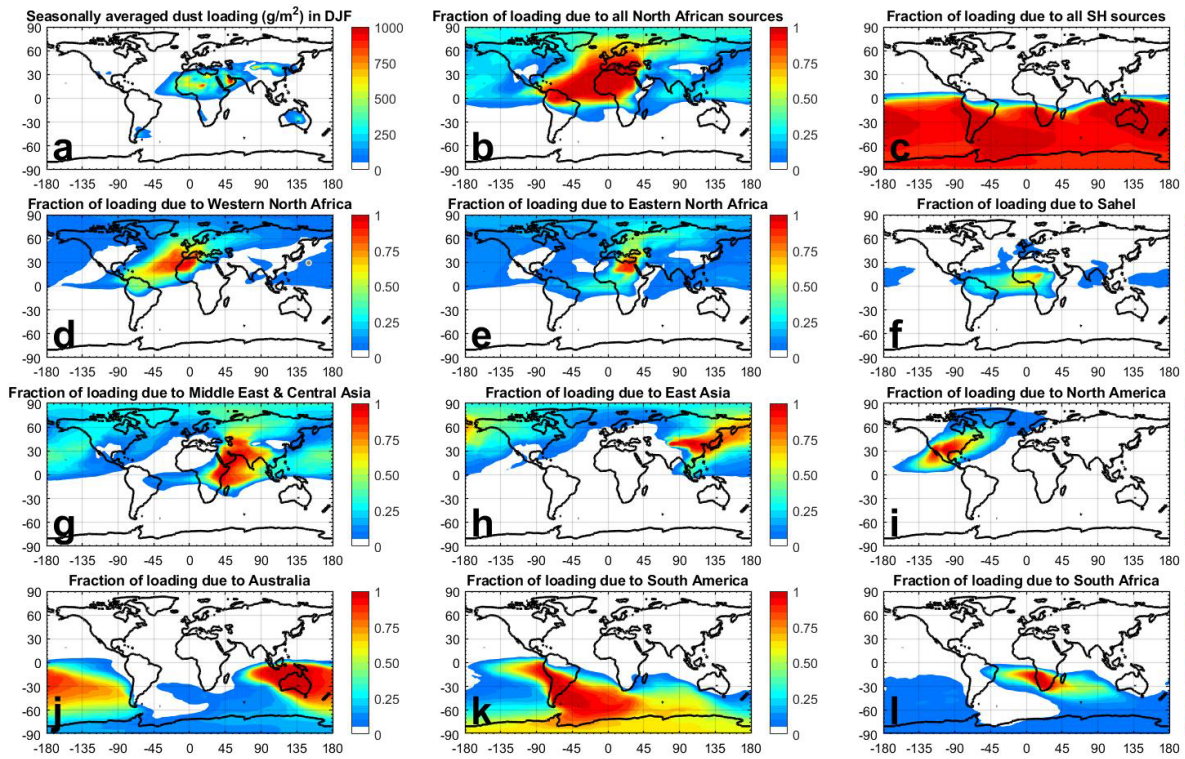
Figure S16. Attribution of the seasonally-averaged PM$_{20}$ dust loading to the world's main source regions in boreal Winter (DJF). Panel ordering is identical to Figures S12-S15.
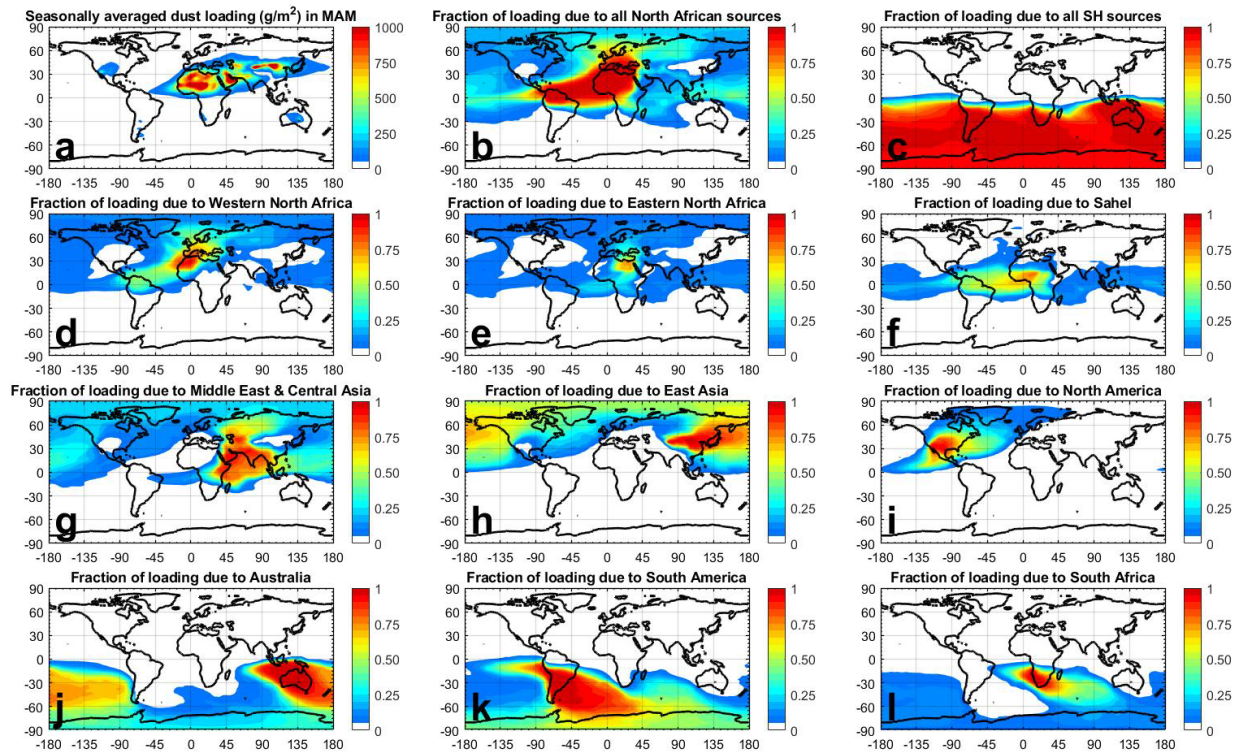
Figure S17. As in Figure S16, but for the attribution of the PM$_{20}$ dust loading in boreal Spring (MAM).
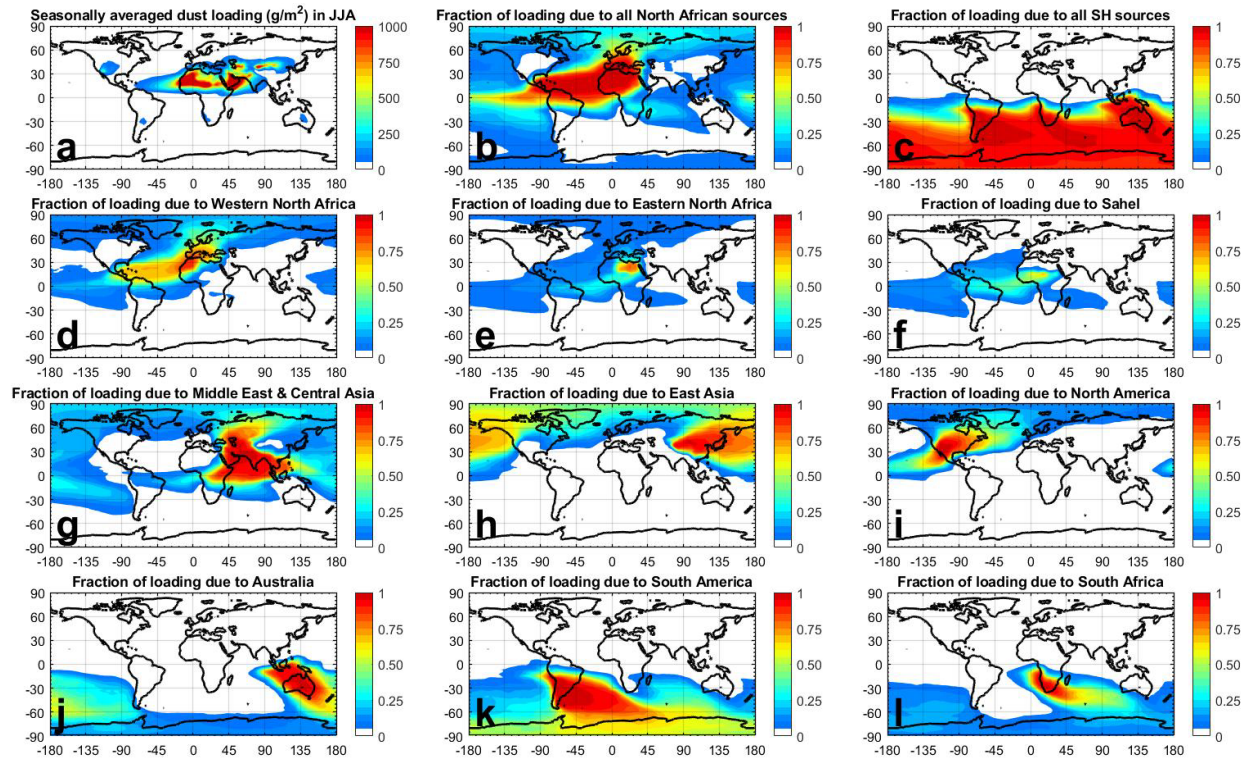
Figure S18. As in Figure S16, but for the attribution of the PM$_{20}$ dust loading in boreal Summer (JJA).
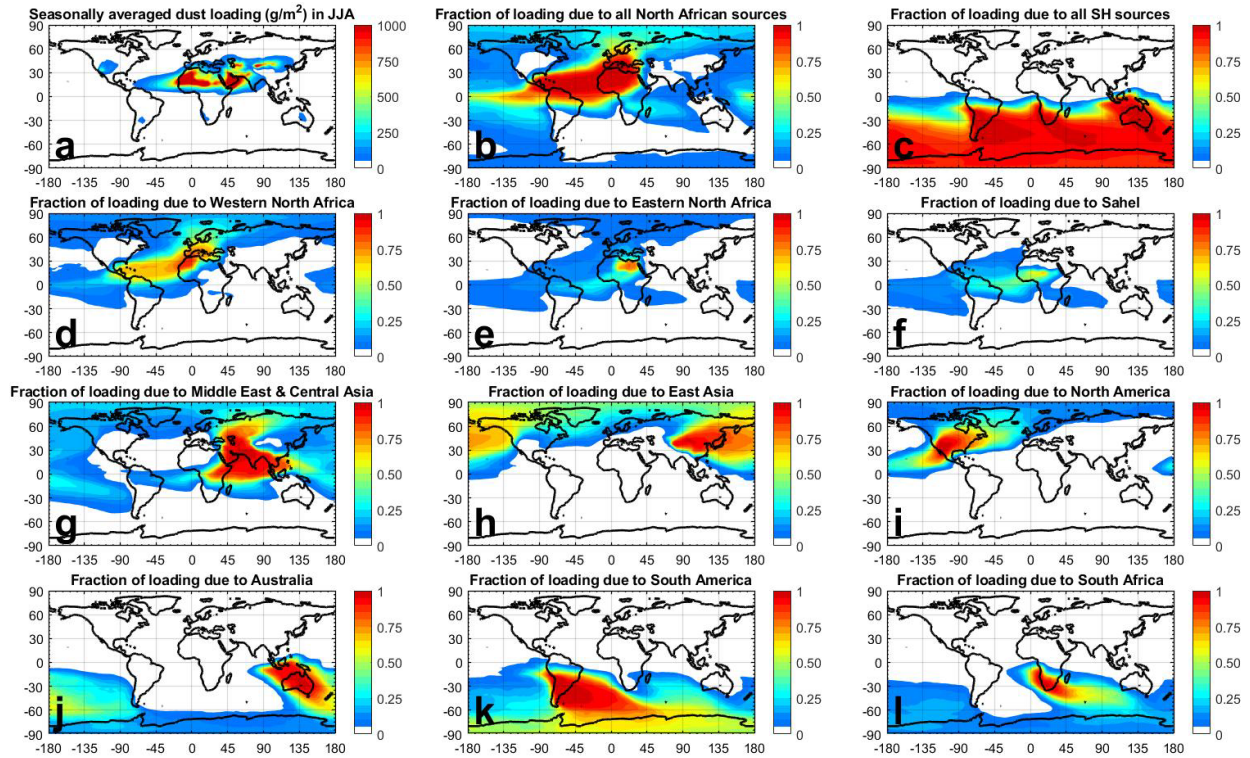
Figure S19. As in Figure S16, but for the attribution of the PM$_{20}$ dust loading in boreal Fall (SON).
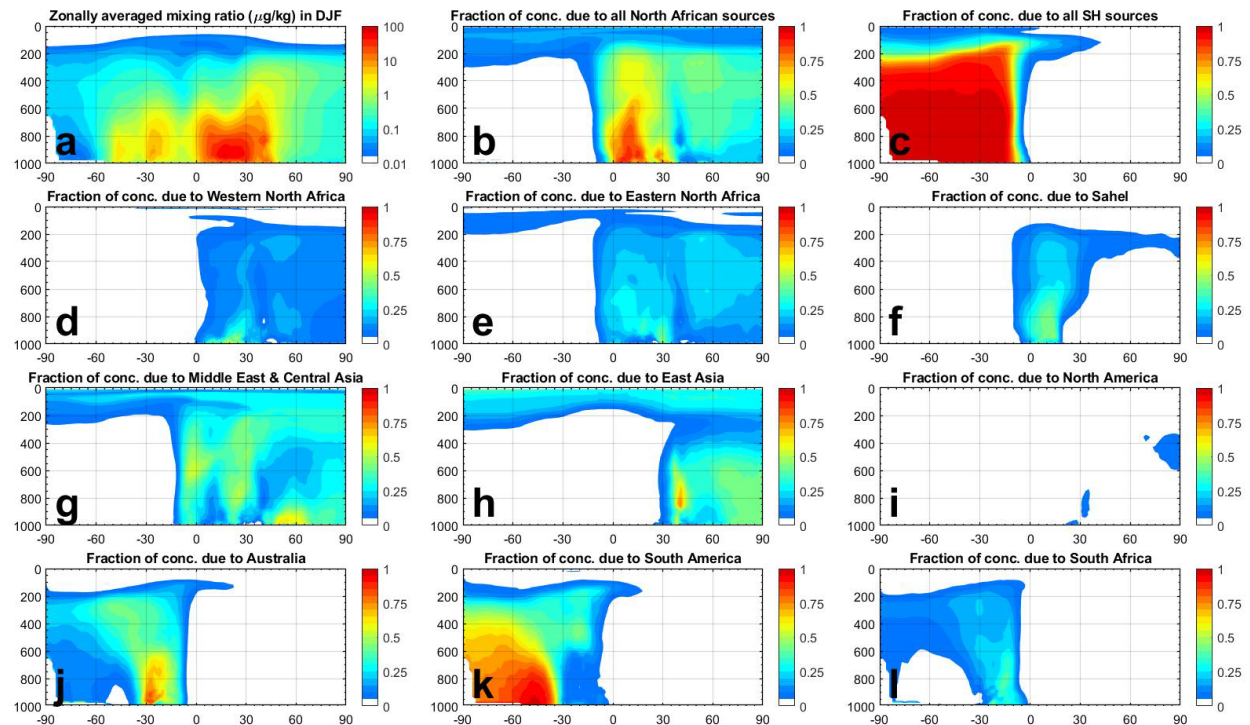
Figure S20. Attribution of the zonally averaged PM$_{20}$ dust concentration to the world's main source regions in boreal Winter (DJF). Panel (a) shows the dust mixing ratio (dust concentration normalized by air density) as a

function of latitude (horizontal axis) and pressure in hPa (vertical axis). Panels (b)-(l) show the partition of the dust concentration per source region, with panel ordering identical to Figures S12-S19.
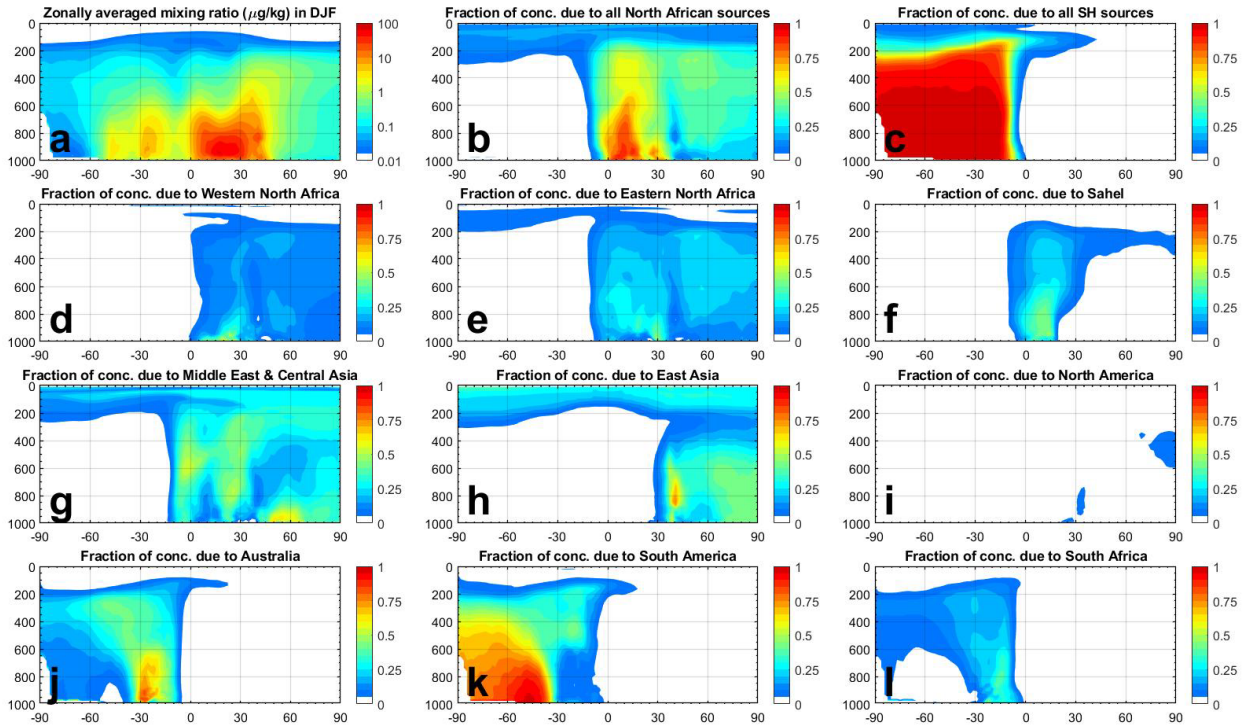
Figure S21. As in Figure S20, but for the attribution of the zonally-averaged PM_{20} concentration in boreal Spring (MAM).
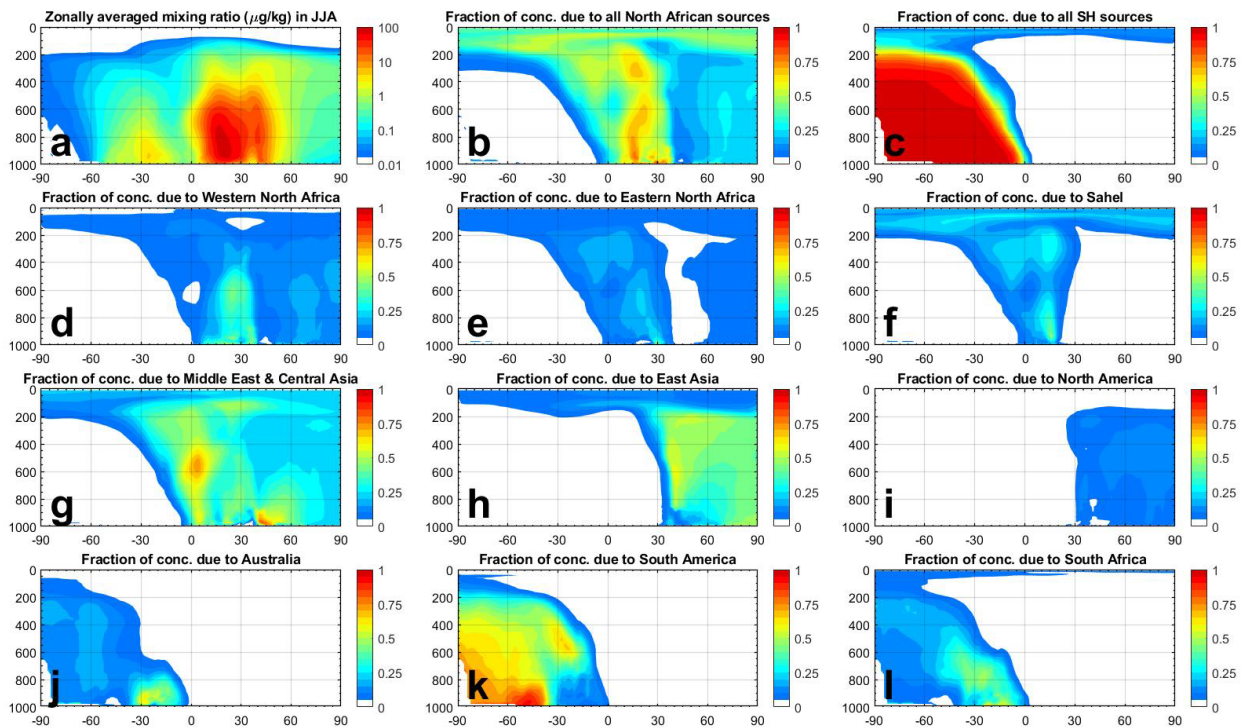

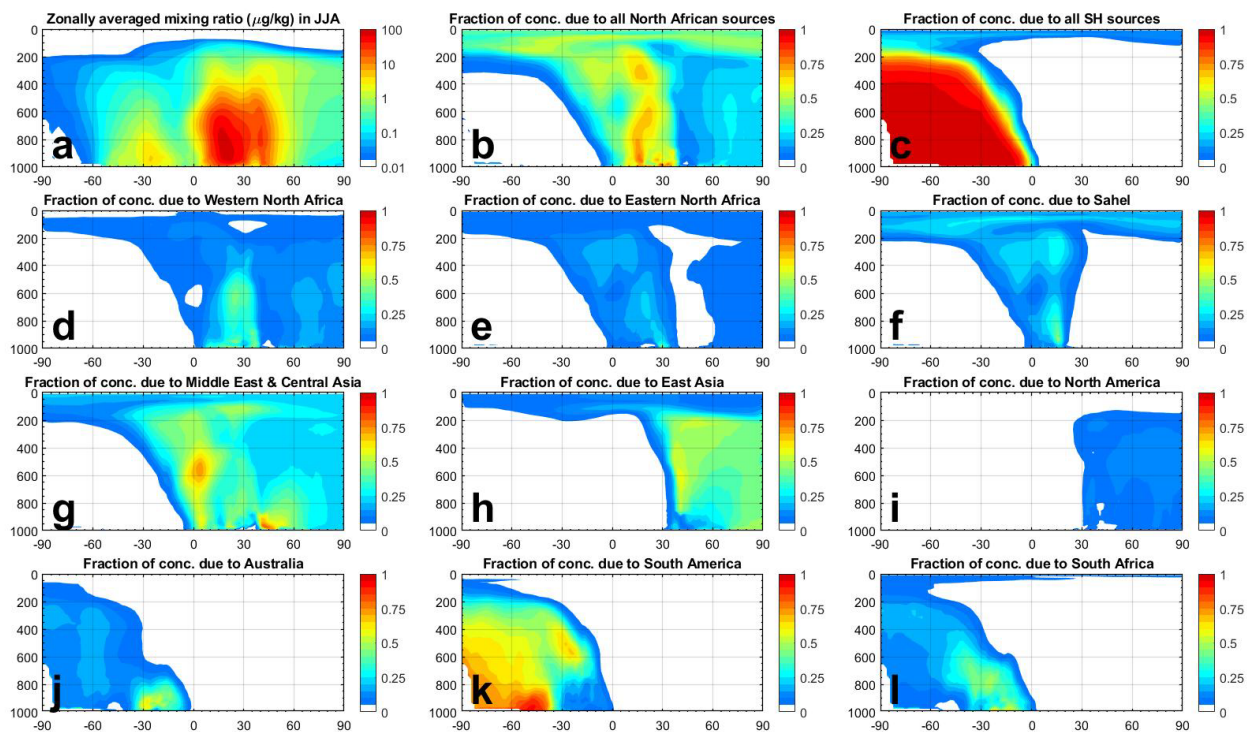**Figure S22.** As in Figure S20, but for the attribution of the zonally-averaged PM_{20} concentration in boreal Summer (JJA).

Figure S23. As in Figure S20, but for the attribution of the zonally-averaged PM$_{20}$ concentration in boreal Fall (SON).
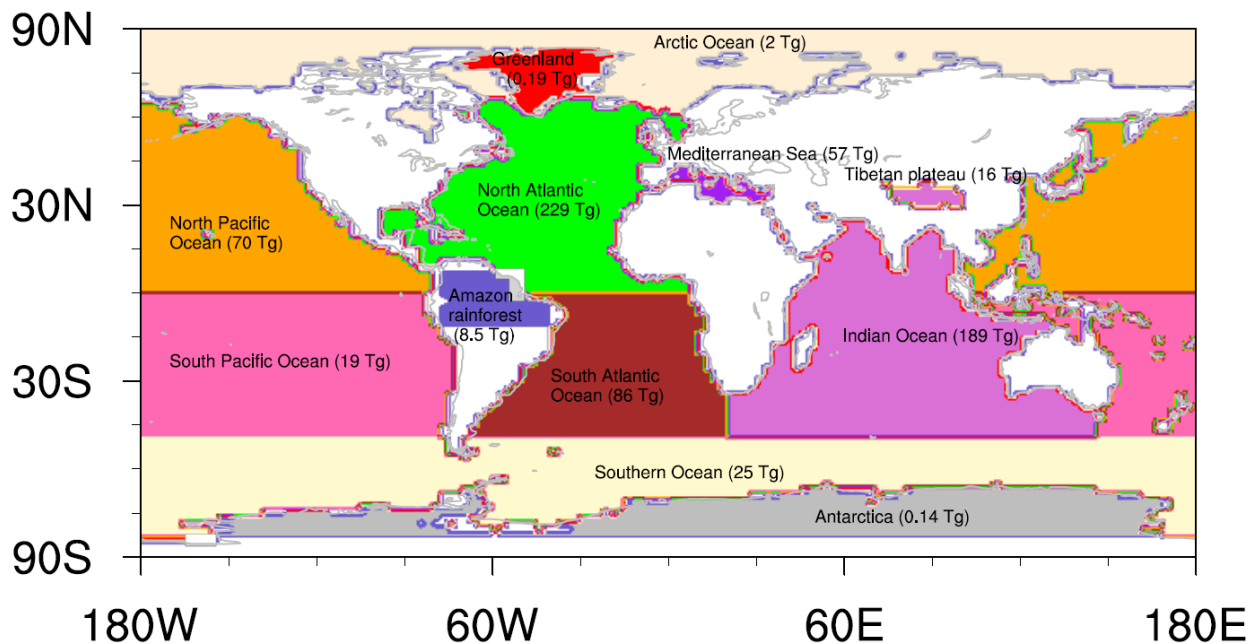

Figure S24. Map of regions to which deposition fluxes are quantified in the main text (Tables 2 and 3), which include the world's ocean basins, as well as terrestrial regions for which dust deposition is particularly important, namely the Amazon rainforest, Greenland, Antarctica, and the Tibetan Plateau. The median estimate of the annual deposition flux to each region is also noted.
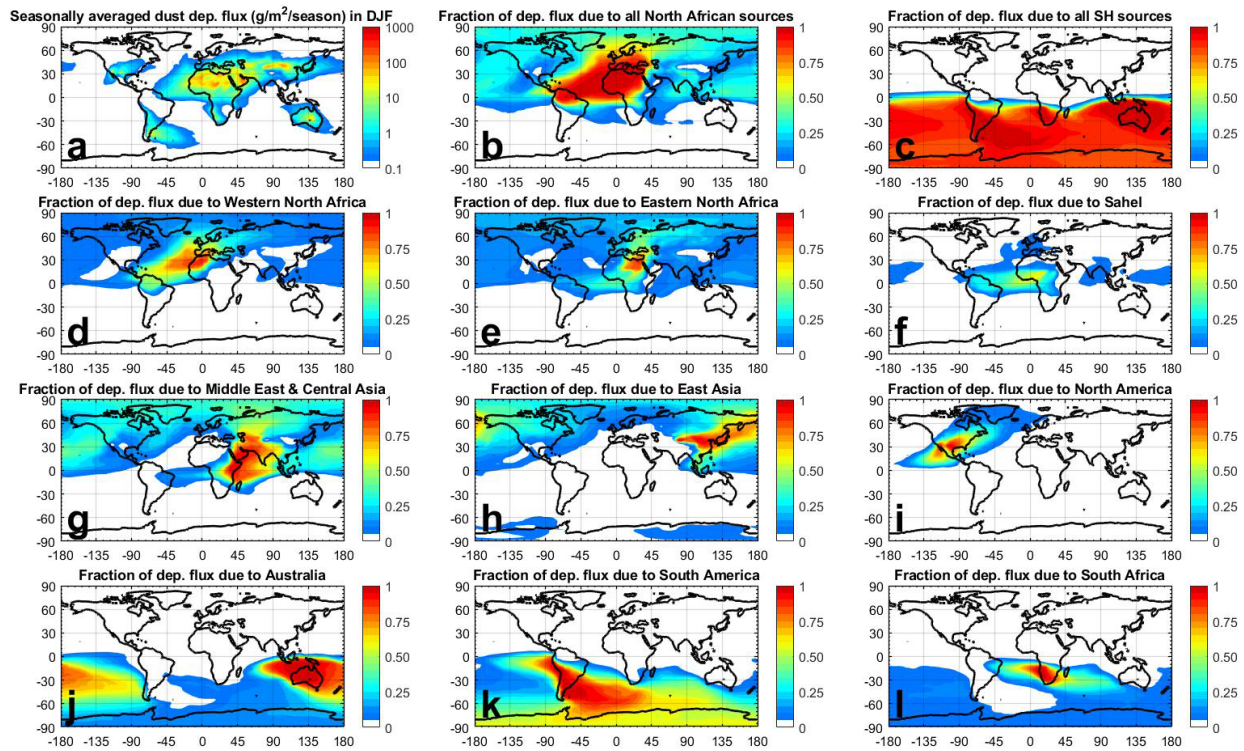
Figure S25. Attribution to the world's main source regions of the seasonally-averaged PM20 dust deposition flux in boreal Winter (DJF). Panel ordering is identical to Figures S12-S23.
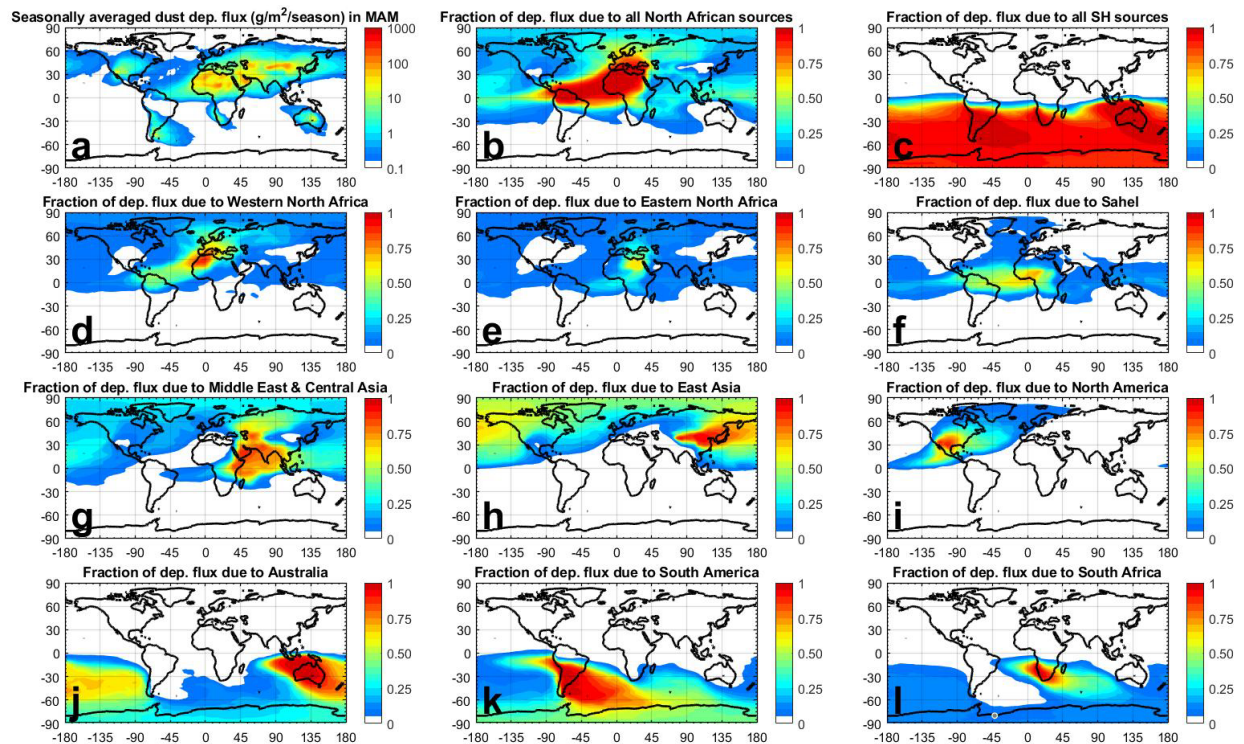
Figure S26. As in Figure S25, but for the attribution of the PM$_{20}$ dust deposition flux in boreal Spring (MAM).
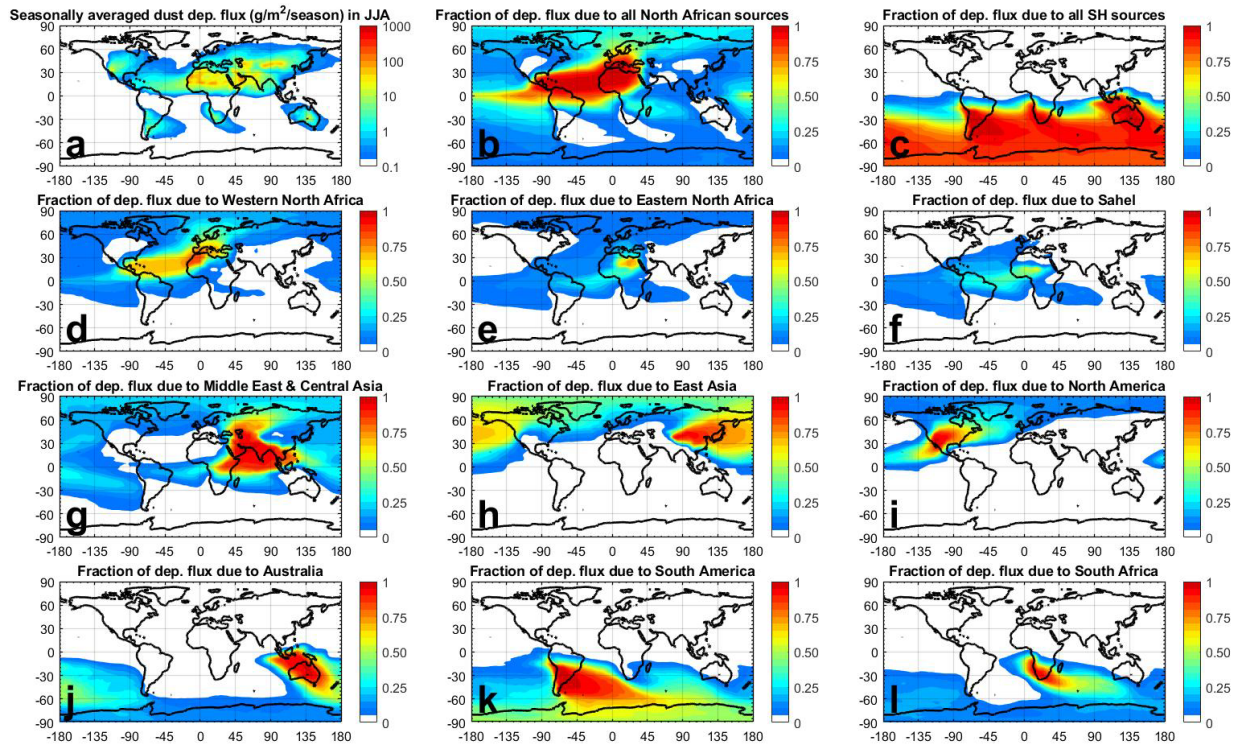

Figure S27. As in Figure S25, but for the attribution of the PM$_{20}$ dust deposition flux in boreal Summer (JJA).
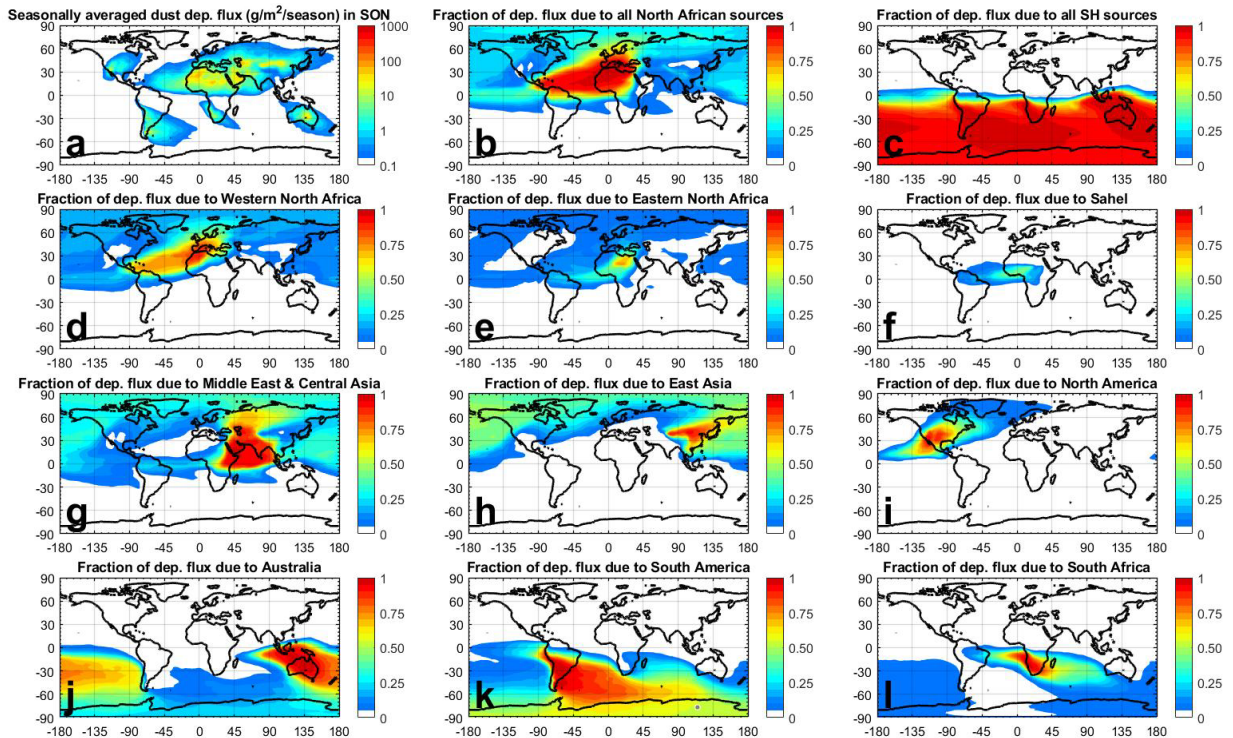
Figure S28. As in Figure S25, but for the attribution of the PM_{20} dust deposition flux in boreal Fall (SON).
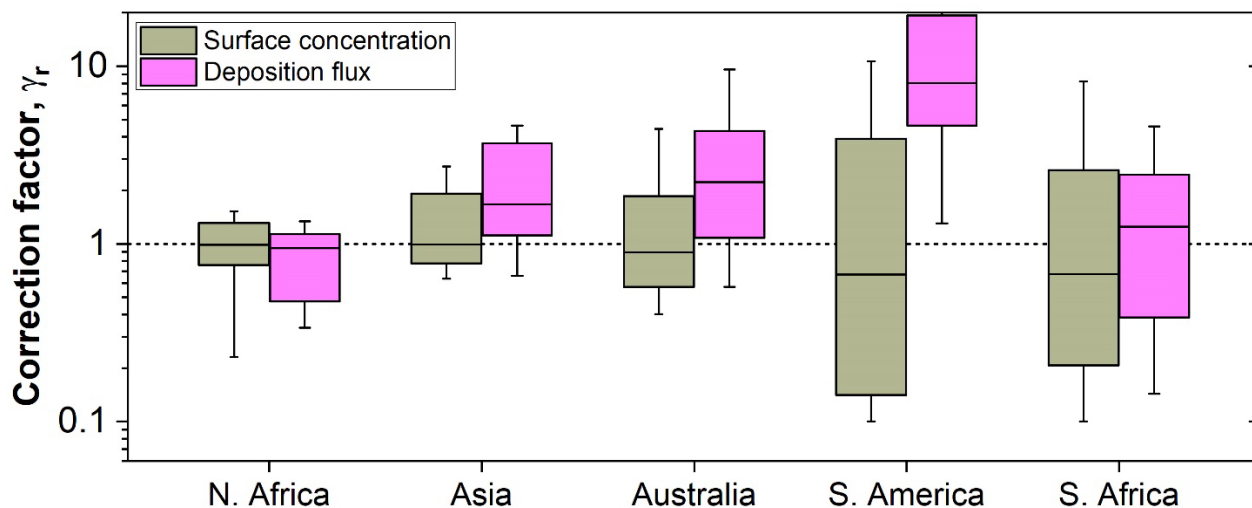

Figure S29. Correction factors needed per source region to optimize agreement against compilations of surface concentration (dark yellow bars) and deposition flux measurement (pink bars), calculated using Eq. (S.7). Box boundaries and whiskers respectively denote the 68% and 95% probability range, and horizontal solid lines denote the median result.

References

Kok, J.F., et al., 2021. Improved representation of the global dust cycle using observational constraints on dust properties and abundance. Atmos. Chem. Phys. in press.